ULTRA-SENSITIVE BROADBAND RECEIVER FOR LONGWAVE RADIO RECEPTION

A Thesis
Presented to
The Academic Faculty

By

Baris Volkan Gurses

In Partial Fulfillment
of the Requirements for the
Undergraduate Research Option in the
School of Electrical and Computer Engineering

Georgia Institute of Technology

May 2020

ULTRA-SENSITIVE BROADBAND RECEIVER FOR LONGWAVE RADIO RECEPTION

Approved by:

Dr. Morris Cohen, Advisor
School of Electrical and Computer Engineering
Georgia Institute of Technology

Dr. Greg Durgin
School of Electrical and Computer Engineering
Georgia Institute of Technology

Date Approved: May 1, 2020

To my parents

Fatma and Levent

ACKNOWLEDGEMENTS

I would like to express my immense gratitude to my advisor, Prof. Morris Cohen, without whom this thesis could not be possible. I am thankful to him for giving me the extraordinary opportunity to lead a research project on my own when I was just a first-year undergraduate student. Since then, he mentored and supported me throughout various stages of my undergraduate career and in my graduate applications. With his tremendous support and mentorship, I gained the experience and skills to pursue a Ph.D. degree with the full confidence and drive to conduct groundbreaking research. Furthermore, I would like to share my gratitude to Prof. Greg Durgin, whose teaching and mentorship boosted me through various challenges of this project.

I would like to thank all of the current and former members of the LF Radio Group for creating an inclusive environment that made me feel like a graduate student in between my undergraduate classes. I am grateful to Kevin Whitmore, Ted Slevin, Charles Topliff, Shweta Dutta, David Richardson, Marc Higginson-Rollins, Nate Opalinski, Nikhil Pailoor, Roderick Gray, Jackson McCormick, and Parker Singletary for their friendship. I would like to specifically acknowledge Kevin Whitmore, who worked with me to build, test, characterize, and deploy this receiver, for his great help and thoughtful conversations throughout this project.

I am eternally indebted to my parents, Fatma and Levent, whose love, support, and sacrifices set me on the path to achieve my dreams. Without their guidance and support, I would not be the person I am today.

TABLE OF CONTENTS

LIST OF TABLES

LIST OF FIGURES

CHAPTER 1
INTRODUCTION

Longwave radio science has been a prominent field for well over a century. While longwave spectrum encompasses numerous bands–including ELF (extremely-low-frequency) (300 Hz-3 kHz), VLF (very-low-frequency) (3-30 kHz), LF (low frequency) (30-300 kHz), and MF (medium frequency) (300 kHz-3 MHz)–, we define longwave as any frequency below 1 MHz. Longwaves, also referred in this thesis as LF waves, are utilized in various applications due to the relatively low attenuation they experience inside both dielectric and conductive materials. Low attenuation is a characteristic of their low frequency, which also allowed the first detection of LF waves.

First detection of natural LF waves was serendipitously made in late 19th century by early telegraph line operators when LF emissions from lightning audibly coupled into long telephone and transmission lines [1]. They were named clicks, grinders, and sizzles due to the sounds heard by the operators as they coupled into the lines. More deliberate experiments were then conducted to study the nature of these LF waves. First such attempt was made by A. S. Popov in 1895 using a long vertical wire connected to an early radio detector. By observing the LF waves detected by his apparatus, he saw a direct correlation between lightning flashes and LF emissions. Similar experiments were carried out in the following decade that resulted in similar conclusions. By the end of 19th century, natural LF waves were positively correlated with numerous atmospheric events such as cyclones, polar fronts, and thunderstorms [2].

While these developments were taking place in the reception of LF radio, great strides were also being made in the transmission of LF waves. After the conception of the idea to utilize radio waves to transmit information over space, Guglielmo Marconi's famous spark gap experiments made breakthroughs in the range of wireless radio transmissions.

First breakthrough happened in 1895 when Marconi grounded a spark-gap oscillator and connected it to an elevated wire antenna. With this setup, he was able to break the 0.5 mile range that was theorized to be the upper limit for how far successful radio transmissions could take place. Second breakthrough happened in 1901 when Marconi used his spark-gap transmitter in Cornwall, England to transmit the letter ”s” in Morse code over the Atlantic Ocean and this transmission was disputably received by a 150-m kite supported antenna in Newfoundland, Canada. While the exact frequency of this transmission wasn't recorded, it is believed to be around 800 kHz. Marconi assumed that his transmitted radio waves were guided by the Earth itself. In his experiment, the radio waves actually propagated across the Atlantic being guided by the charged particles in the atmosphere acting as a conductor and the Earth which operated as a ground plane. This transatlantic radio transmission marked the beginning of using LF radio as a form of long-range wireless communications [3] [4].

Following these breakthroughs, the reception and transmission of LF radio became an active research area that gathered great interest. The radiotelegraphy era saw the modulation of LF radio waves to enable worldwide wireless communications in the early 19th century. This boosted the significance of LF radio as LF radio transmitters and receivers became commonplace especially through World War I and World War II.

Military applications have also seen great interest in LF radio. In addition to LF military communications, LF waves were used for navigation purposes during World War II and thereafter. Decca Navigation System was invented in the US and implemented by the Royal Navy of the UK to be used by Allied forces during World War II. Utilizing VLF transmitters, Decca allowed accurate long-range positioning by comparing phase delays of two single-frequency signals at 70 and 130 kHz. Decca remained in both military and civilian use for the rest of the century [5]. A similar system, named ”Datatrak”, was used for commercial applications and operated in frequencies between 125 and 150 kHz [6]. LORAN-C utilized another method for navigation using LF transmitters emitting short pulses at 100 kHz. Comparing the times of the received pulses emitted by different trans-

mitters, LORAN-C could accurately geolocate the receiver [7]. A breakthrough for global positioning was made by the Omega system established by the US. Omega utilized a network of VLF transmitters that operated between 10 and 14 kHz to enable accurate geopositioning all around the globe [8]. A similar system, named "Alpha", is currently still in use by Russia. Despite slowly being decommissioned, Nationwide Differential GPS (NDGPS) network in the US still uses LF in frequencies between 285-325 kHz to broadcast correction messages to compensate for the errors added by ionospheric effects to GPS signals and enhance the accuracy of GPS [9].

LF radio has also been widely used for wireless communications between navy submarines and ground stations since LF waves can penetrate seawater 10s of meters deep because of skin effect. Numerous LF radio beacons have been built and deployed by multiple countries to establish continuous communication links with submarines underwater globally. These beacons utilize individual physically large antennas or arrays of physically large antennas with a diameter usually on the order of kilometers. These transmitting antennas are usually umbrella top-loaded monopoles to increase the radiation resistance as much as possible for the best radiation efficiency [10] [11]. On the receiving side, submarines host physically and electrically small antennas in the form of either loop or dipole antennas. Due to their electrically small size, these antennas cannot transmit power efficiently but can be used to receive the immense amount of power radiated by the beacons [12]. Similar to seawater, LF waves can also penetrate rock and soil 10s of meters deep. For that reason, LF radio is also used for subterranean imaging, radiolocation, and through-the-earth mine communications.

After the first detection of natural LF waves, more discoveries have been made regarding the correlation between lightning and LF radio. When a lightning event occurs, an ionized channel between two charged regions of the atmosphere forms. This ionized channel acts as an electromagnetic source and an antenna kilometers long. During such a discharge event, up to one GJ of power is released in the form of electromagnetic radia-

tion as well as shock waves, or thunder, caused by atmospheric gasses experiencing huge increases in pressure and expanding outwardly that can be heard miles away. Although between 0.01% and 1% of this energy is released electrically, a short burst of broadband electromagnetic waves of great intensity, whose frequencies can range from a few Hz to the optical band, is radiated omnidirectionally [13]. However, most of this electromagnetic energy is radiated in frequencies between 1 and 100 kHz and reflects off the lowest layers of the ionosphere [14]. By reflecting off both ionosphere and ground, these LF waves, colloquially named radio atmospherics or sferics, emitted by lightning propagate globally in this Earth-ionosphere waveguide (EIW) with low attenuation (around 3 dB per 1000 km) [15]. This low attenuation allows sferics to propagate globally setting the atmospheric noise floor, which is the noise floor considered in the system design of non-scientific applications summarized above. However, since this noise floor is filled with pulses of LF waves from lightning, the atmospheric noise floor can be modeled as a Poisson arrival process instead of white Gaussian noise [16]. Detecting sferics with even a sparse network of LF receivers hundreds of kilometers apart also enables lightning geolocation at a global scale [17]. This allowed sophisticated LF networks to be put in use for global monitoring of where and when lightning occurs.

Transient luminous events (TLEs) such as lightning are not the only sources of LF waves propagating in the EIW. Aforementioned man-made LF transmitters also pump LF waves into the atmosphere that then propagates globally in the EIW. Therefore, emissions in the LF spectrum can be crudely characterized as short bursts of broadband sporadic spikes–sferics–along with narrowband continuous signals. However, as these emissions propagate in the EIW, they do not reflect off the waveguide boundaries unaffected. As they reflect off the ground, some power is dissipated in the ground depending on the surface conditions. Similarly, as they reflect off the ionosphere, some power escapes through and follows the magnetic field lines of the Earth [14]. These so-called whistlers, named after the sounds they make as they couple into the telephone and telegraph lines, eventually go

back through the atmosphere again on the other end of the magnetic field line and can be detected by a sensitive receiver. As these waves propagate through the ionosphere and near-Earth space environment, detecting them is useful for global monitoring the state of these environments without any need for satellites or sounding rockets.

Even a more useful diagnostic for monitoring the ionosphere and near-Earth space environment is detecting the remaining power that is trapped in the EIW. As these waves interact with the lowest layers of the ionosphere, their waveforms are altered. However, these alterations are sensitive to the state of the ionosphere, which is affected by various terrestrial and celestial events, including but not limited to, solar flares, general solar x-ray activity, solar eclipses, astronomical gamma-ray bursts, lunar tides, geomagnetic storms, and lightning [18]. How these events affect the ionosphere can be monitored by detecting and analyzing the propagation of the LF waves in the EIW. This monitoring is named ionospheric remote sensing, and it is a powerful diagnostic tool in geoscience and radio science.

LF receivers undeniably enable numerous applications LF waves can be used for. Since they are the first node in the data acquisition and analysis, minimum amount of information extracted from the physical system is set by the hardware performance of the receivers. While the hardware performance have several key characteristics that improve how much and how easy the information can be extracted from the recorded data, the most significant parameter is the system sensitivity. Sensitivity of a system is usually defined as the minimum signal a sensor needs to be subjected to to have its output have a specific signal-to-noise ratio (SNR). Lowering this parameter improves the quality of the data that is recorded by the sensing system, and most LF receiver designs strive to improve this parameter especially in remote sensing applications.

Ultra-sensitive LF receivers have become more sophisticated as new data processing techniques, storage fabrication technologies allowed ultra-low-noise components and devices readily available for system use. Modern LF receivers can be categorized as mag-

netic field receivers and electric field receivers. Magnetic field receivers utilizes induction to couple LF waves propagating in the environment. Most notable LF magnetic field receiver designs include the AWESOME receiver developed at Stanford University and the Georgia Institute of Technology. Multiple iterations of the AWESOME receiver have been developed, but the most recent iteration has a minimum sensitivity of 0.03 $\mathrm{fT}/\sqrt{\mathrm{Hz}}$ with an operating frequency range between 0.5 kHz and 500 kHz [18]. Designs of other iterations of the AWESOME receiver can be found in [19], [20], and [21]. Other compact LF magnetic field receiver designs have also been developed to be used in satellites for space research. One of these designs achieve a minimum sensitivity of 4 $\mathrm{fT}/\sqrt{\mathrm{Hz}}$ with a frequency range between 1 Hz and 20 kHz [22]. Another notable design is presented in [23].

Electric field receivers, on the other hand, utilizes conduction to detect LF waves. There has been fewer attempts to design an electric field receiver due to its challenging calibration and heavy dependence of the successful operation of the receiver on a precise circuit design that minimizes current noise throughout the front-end. However, one notable electric field receiver design is shown in [24]. An early LF instrument that utilizes a combination of both electric field and magnetic field sensors is also presented in [25]. Finally, a comprehensive report of LF receiver design methods and trade-offs are described in [26]. In this thesis, we describe a novel electric field receiver system that achieves unprecedented sensitivity with broadband reception capability. While magnetic field receivers are conventionally used for LF radio reception, electric field receivers unearth valuable information that cannot be extracted by magnetic field receiver. One such application is in the near-field characterization of LF sources. Some harmonics that can't be picked up by magnetic field receivers can be picked up by electric field receivers in the near-field region of an LF source, possible enabling untapped applications of LF remote sensing. Other numerous applications are also enabled by simultaneous magnetic and electric field recordings such as resolving the phase ambiguity in lightning geolocation networks [17] and sensing and imaging through

conductive media. An early iteration of this electric field receiver design can also be found in [27] and [28].

The thesis is structured as follows: Section 2.1 describes the system architecture and components in detail. Section 2.2 introduce two calibration methods used to calibrate the receiver system. Lastly, Section 3.1 shows the frequency response and sensitivity of the receiver characterized empirically.

CHAPTER 2
METHODOLOGY

2.1 System Architecture

The electric field receiver is comprised of two main parts, the front-end and the back-end. The front-end contains a dipole antenna and two preamplifiers. The dipole antenna is directly attached to the first preamplifier, named as Pre2amp, which includes a custom ultra-low-noise differential amplifier (ULNA) and driver. Pre2amp is connected to the second preamplifier, named as Preamp, via a Cat5e ethernet cable with three 100-Ω shielded and twisted pairs. Preamp includes low and high-pass filters, an attenuator, and a driver to drive the signal to the back-end. Preamp can be mounted on a backplane card in a metal box along with two other cards, allowing the electric field receiver to be used simultaneously with two channels of another receiver–such as two channels of data coming from the two orthogonal loop antennas of a magnetic field receiver.

The back-end contains a line receiver and data storage unit with a recording software. The line receiver has a GPS synchronization circuitry, anti-aliasing filter, an instrumentation amplifier, and an analog-to-digital converter (ADC). After the incoming data from the front-end is processed by the line receiver, the data is sent to the data storage unit, usually in the form of a computer, and the data recording software saves the data.

The front-end and back-end are connected via a specialized audio cable (1217B) made by Belden with four 75-Ω twisted and shielded pairs that drives the signals from the front-end to the back-end and power from the back-end to the front-end.

Top left panel of Fig. 2.1 shows Pre2amp with a connected dipole antenna. Middle left panel shows Preamp mounted on a backplane with two preamplifier cards of a magnetic field receiver, all enclosed in a metal box. Top right panel shows front-end waterproof

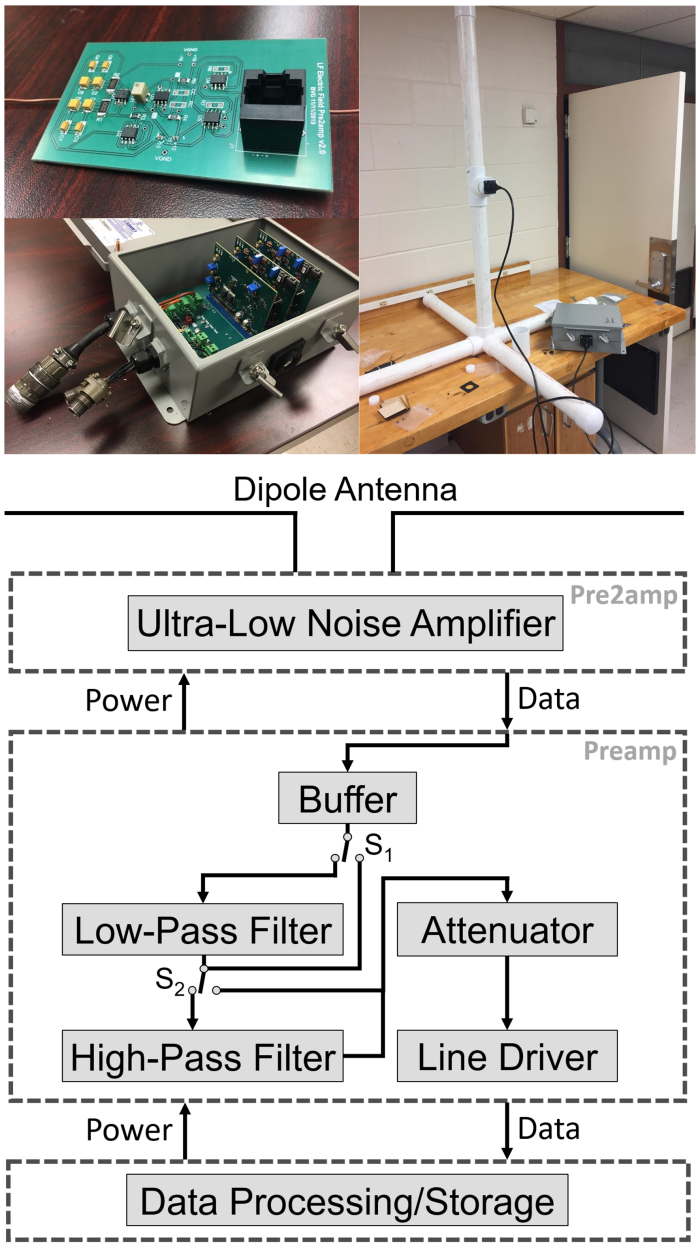

Figure 2.1: Photographs and block diagram of the electric field receiver.

setup showing Pre2amp with dipole in a PVC pipe connected to the Preamp box via a Cat5e ethernet cable. Lastly, bottom panels displays the block diagram of the receiver showing the system workflow. In the block diagram, switches, S_1 and S_2, represent the configurable mechanism that enable and disable the Preamp filters and reroute the signal path based on the desired frequency response for data collection.

Now, we will go on to explain each system component described in this summary in

more detail.

2.1.1 Antenna

Different types of antennas are suited better for the detection of either electric or magnetic field components of the LF radio waves. Magnetic field receivers usually employ ferrite-core or air-core loop antennas, whereas electric field receivers usually use monopole or dipole whip antennas. A key characteristic for the antenna design is antenna sensitivity. For both electric and magnetic field antennas, we define the antenna sensitivity as the field equivalent of the antenna noise, namely a normally incident field that would induce the same open circuit voltage as the antenna noise over a 1 Hz bandwidth. Hence, we broadly derive the antenna sensitivity for any antenna as

$$S_a = \frac{V_n}{G_a} \tag{2.1}$$

where V_n is the antenna noise spectral density, and G_a is the open-circuit voltage gain of an antenna in a system, shown in Fig. 2.2. This definition describes the lowest field magnitude an antenna can receive before it is dominated by the antenna noise. We will now derive the antenna sensitivity expressions for both electric and magnetic field antennas and compare them to argue which antenna offers lower, namely better, sensitivity for the receiver.

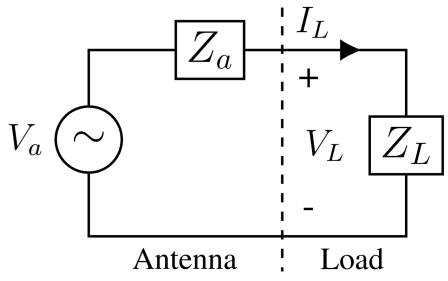

Figure 2.2: Equivalent circuit model of an arbitrary receiving antenna in a system.

Coupling of incoming waves to magnetic loop antennas is governed by Faraday's law of induction. Electromagnetic waves induce a time-varying electric potential across the an-

tenna terminals. At low-frequencies, the induced open-circuit voltage can be approximated as $V_a = j\omega N_a A_a B_i cos(\theta)$, where N_a is the number of turns, A_a is the loop area, B_i is the magnetic flux density, and θ is the angle of incidence of the incoming wave. This approximation is valid due to LF waves' long wavelengths compared to the loop antenna's size. Assuming that the incoming wave satisfies the far-field conditions, (i.e. $E_i/B_i = c$), and is normally incident to the loop, we can derive the open-circuit voltage gain of any loop antenna as $G_a = \frac{V_a}{E_i} = \frac{2\pi N_a A_a}{\lambda}$, where λ is the wavelength and E_i is the electric flux density. To derive the voltage noise spectral density of the loop, we need to define the antenna resistance. Loop resistance is the sum of the loop's radiation resistance and loss resistance. Due to the low radiation resistance at low frequencies, antenna resistance is dominated by the loss resistance, defined as $R_a = \rho\frac{4L}{\pi d^2}$, where ρ is the wire resistivity, L is the wire length, and d is the wire diameter. Johnson-Nyquist or thermal noise of this resistance is $V_n = \sqrt{4k_B T R_a}$. Thus, we can derive the loop antenna sensitivity as

$$S_a = \frac{2\lambda}{\pi d N_a A_a}\sqrt{\frac{k_B T \rho L}{\pi}} \tag{2.2}$$

(2.2) shows that for differently-shaped loop antennas with the same N_a, the shape that has the lowest $\sqrt{L}/A_a$ offers the lowest sensitivity. This shape is a circle with a $\sqrt{L}/A_a$ of $3.54/N_a$. For comparison purposes, we will be using a circular loop antenna, meaning $A_a = \frac{L^2}{4\pi N_a^2}$. Therefore,

$$S_a = \frac{4N_a\lambda}{Ld}\sqrt{\frac{k_B T \rho}{L\pi}} \tag{2.3}$$

Another step that will improve this expression is to relate the sensitivity to the two critical characteristics for receiver deployment, antenna weight and size. Antenna weight can be expressed by the mass of the antenna, calculated as $M_a = \frac{1}{4}\pi d^2 L\delta$, where δ is the wire density. Antenna size can be expressed by the height of the antenna, defined as $h_a = \frac{L}{\pi N_a}$.

Hence, rewriting (2.3) as a function of height and mass,

$$S_a = \frac{2d\delta\lambda}{M_a}\sqrt{\frac{k_B T \rho N_a}{h_a}} \tag{2.4}$$

We can do the same derivation for an electric field antenna, relating its size and weight to its sensitivity. Time-average power of an incident traveling wave is calculated as $\overline{P_i} = \frac{E_i^2}{2\eta}$, where E_i is the incident electric field amplitude and η is the intrinsic impedance of the medium. Coupling of this power to the antenna is calculated as $P_a = \overline{P_i} A_{em}$, where A_{em} is the antenna aperture. For any antenna, antenna aperture is defined as $A_{em} = \frac{\lambda^2 D R_r}{4\pi R_a}$, where D is the antenna directivity and R_r is the antenna radiation resistance. For low-loss conductive antennas in free space, the antenna resistance can be modeled as the radiation and loss resistances in series with each other, $R_a = R_r + R_{loss}$. Loss resistance of a short dipole and monopole at low frequencies is the same as that of a loop antenna, namely $R_{loss} = \rho\frac{4L}{\pi d^2}$. Radiation resistance of a short dipole and monopole is calculated as $R_r = 20\left(\frac{\pi L}{\lambda}\right)^2$, where L is the total antenna length for both, meaning the radiation resistance of a monopole is half of that of a dipole. Then, in air, coupled power can be calculated as

$$P_a = \frac{E_i^2 \lambda^2 D R_r}{960\pi^2 R_a} \tag{2.5}$$

For a system as shown in Fig. 2.2, the received power by the load is calculated as $P_L = \frac{1}{2}Re\{I_L V_L\} = \frac{1}{2}\frac{V_a^2 R_L}{|Z_a + Z_L|^2}$. Hence, for a conjugate matched load, i.e. $Z_L = Z_a^*$,

$$P_L = \frac{V_a^2}{8R_a} \tag{2.6}$$

Using (2.5) and (2.6), we can derive the open-circuit voltage gain of any electric field antenna given that $P_a = P_L$ for a conjugate matched load.

$$G_a = \frac{\lambda\sqrt{DR_r}}{2\pi\sqrt{30}} \tag{2.7}$$

Substituting $R_r = 20\left(\frac{\pi L}{\lambda}\right)^2$ in (2.7),

$$G_a = L\sqrt{\frac{D}{6}} \tag{2.8}$$

(2.8) shows that the open circuit voltage gain of a short electric field antenna is entirely dependent on the antenna length. Therefore, to maximize the SNR, a longer antenna is desired.

Voltage noise of an electric field antenna is dominated by the thermal noise of the antenna resistance, $V_n = \sqrt{4k_BT(R_{loss} + R_r)}$. However, at very low frequencies (¡20 kHz), loss resistance dominates over the radiation resistance, allowing us to approximate the thermal noise as $V_n = \sqrt{4k_BTR_{loss}}$. Therefore, using (2.1), the electric field antenna sensitivity is derived as

$$S_a = \frac{4}{Ld}\sqrt{\frac{6k_BT\rho L}{\pi D}} \tag{2.9}$$

To include antenna mass and height in this expression, same mass expression for the magnetic field antenna can be used. Furthermore, for a dipole or a monopole, $L = h_a$. Therefore,

$$S_a = \frac{6d\delta}{M_a}\sqrt{\frac{k_BT\rho\pi}{Dh_a}} \tag{2.10}$$

Both electric field and magnetic field antenna sensitivities have the same relation with the antenna mass and height. Therefore, to compare the sensitivities of electric and magnetic field antennas of the same mass and height, we divide (2.10) by (2.4). Thus,

$$S_a = \frac{3}{\lambda}\sqrt{\frac{\pi}{DN_a}} \tag{2.11}$$

This expression gives the ratio of sensitivities of electric field and magnetic field antennas when they have both the same mass and the same height. We can further simplify (2.11) by specifying the electric field antenna directivity. For this, we need to determine whether to use a dipole or a monopole for the electric field antenna. While monopole antennas

have double the directivity of dipole antennas, dipole antennas have other advantages over monopole antennas such as allowing the receiver to have differential architecture, crucial for eliminating common-mode noise in the system. Therefore, we utilized a dipole antenna in this design, allowing us to substitute 1.5 for D. Therefore,

$$SR = \frac{4.342}{\lambda\sqrt{N_a}} \tag{2.12}$$

If this ratio is smaller than 1, electric field antenna sensitivity is shown to be lower than that of magnetic field antenna and vice versa. Frequency sweep of this expression for various N_a is shown in Fig. 2.3.

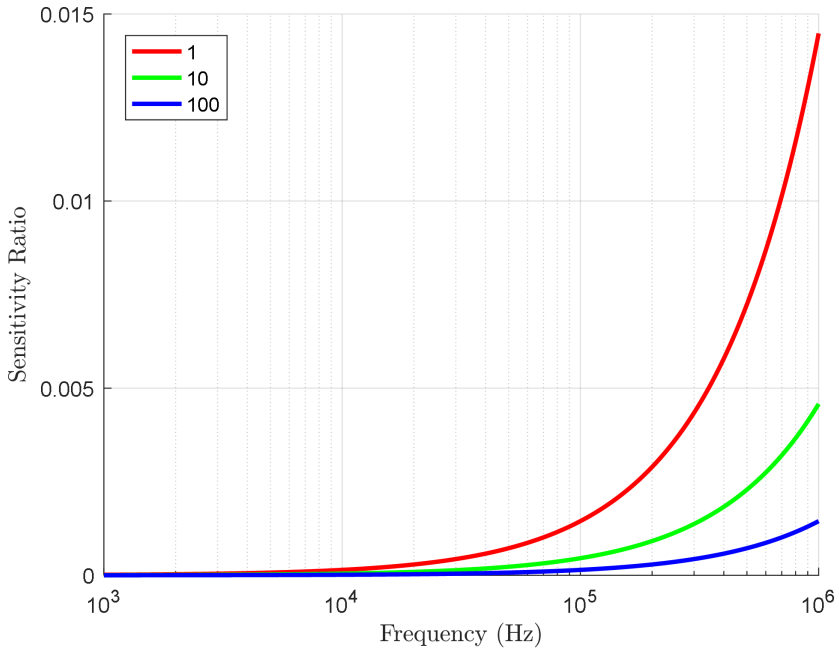

Figure 2.3: Sensitivity ratio of electric field and magnetic field antennas of the same mass and height with varying magnetic field antenna turns.

As seen in Fig. 2.3, electric field antennas have significantly lower sensitivities than magnetic field antennas. Furthermore, sensitivity and gain response of electric field antennas can be further improved by top-loading the antennas and effectively increasing L without changing h_e. The low sensitivity of electric field antennas allows the system sen-

sitivity of electric field receivers to be limited by the amplifier noise rather than antenna noise as is the case for magnetic field receivers [26]. Furthermore, electric field receivers offer the flexibility to lower the system noise by improving the amplifier design with each receiver iteration. For these reasons in addition to the multitudinous applications LF electric field reception enables, we utilize a dipole antenna made out of 16 AWG copper wire. Hence, antenna sensitivity of a dipole antenna at low frequencies is calculated and shown in Fig. 2.4.

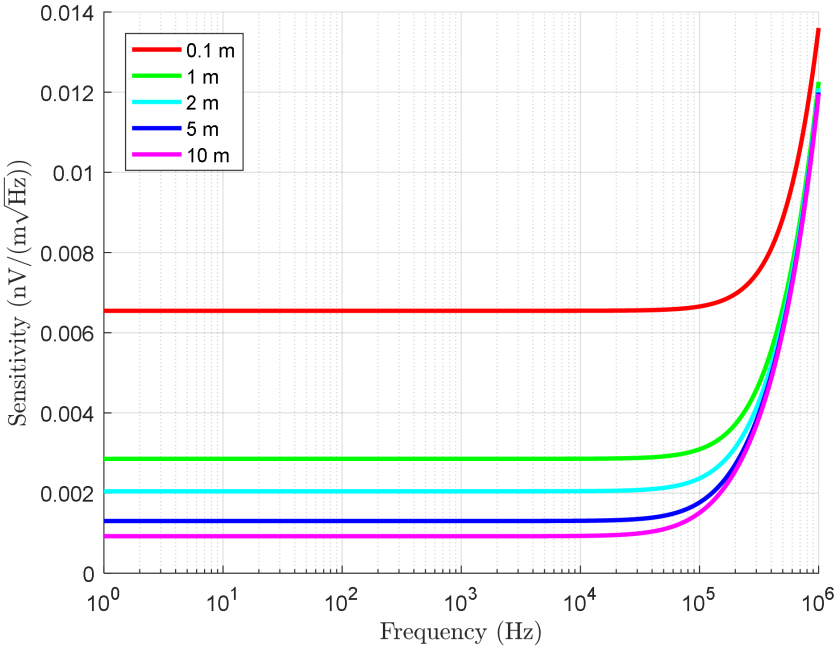

Figure 2.4: Sensitivity of a dipole antenna of varying antenna lengths.

While dipole antennas' sensitivity is substantially lower than that of magnetic loop antennas, another noise source caused by the antenna parameters affects the receiver system noise. Compared to magnetic loop antennas, electric field antennas have significantly higher capacitive reactance at low frequencies. This can be explained by the fact that the induced current distribution in an electrically small dipole antenna is virtually constant. Therefore, seen from the load, the antenna acts as an open circuit. The highly-capacitive reactance of the dipole significantly increases the input impedance causing any current

noise leaking from the amplifier's first stage to add to the system voltage noise. Therefore, for the amplifier design, finding the dipole input impedance is crucial.

To find the dipole input impedance, it is first worthwhile to note that all the expressions we have derived so far assumed far-field conditions. However, deriving an expression for the input impedance of a dipole requires an exhaustive analysis of the near-field conditions. Induced EMF (IEMF) method is one numerical method used to analyse the near-field behavior and derive a closed-form expression of the dipole input impedance as shown in [29]. Defining the input impedance as $Z_a = R_a + jX_a$, we calculate the input resistance and reactance of a dipole antenna,

$$R_a = R_{loss} + R_r = \rho\frac{4l}{\pi d^2} + 20\left(\frac{\pi l}{\lambda}\right)^2 \tag{2.13}$$

$$\begin{aligned} X_a =& \frac{\eta}{4\pi sin^2(\beta l/2)}\left\{2S_i(\beta l) - cos(\beta l)\left[S_i(2\beta l)\right.\right. \\ & - 2S_i(\beta l)) \; + \; sin(\beta l)\left[C_i(2\beta l) - 2C_i(\beta l)\right. \\ & \left.\left. + C_i(\beta d^2/2l)\right.\right. \end{aligned} \tag{2.14}$$

where η is the intrinsic impedance of free space, E is the Euler constant, β is the phase constant, S_i is the sine integral, and C_i is the cosine integral. l is the effective antenna length to account for the gap between the wires of the dipole and is defined as $l = L^2/(L - x)$, where x is the gap distance. For an electrically-small dipole, (2.13) and (2.14) could be approximated as

$$R_a = \rho\frac{4l}{\pi d^2} \tag{2.15}$$

$$X_a = -120\frac{ln(l/d) - 1}{tan(\beta l)} \tag{2.16}$$

For different dipole lengths, input resistances and reactances from (2.13) and (2.14) using IEMF are calculated over the ELF/VLF/LF/MF spectrum. Then, each dipole's method-of-

moments (MoM) model was simulated and compared with the IEMF results in Fig. 2.5. As seen in Fig. 2.5, both models provide fairly consistent results.

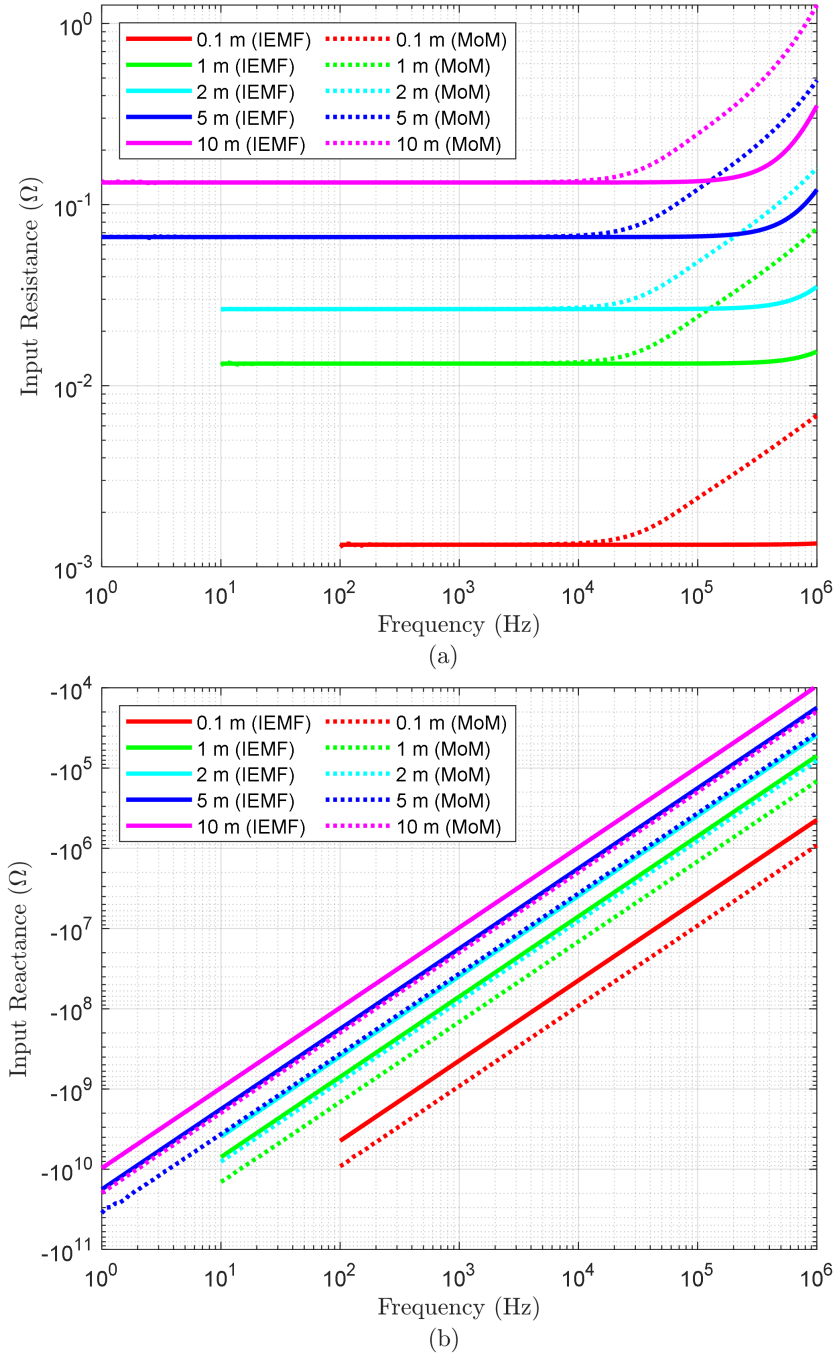

Figure 2.5: Modeled input impedances of dipole antennas of different lengths using IEMF and MoM over frequency. (a) Input resistance. (b) Input reactance.

While these models of a dipole in free space provide us with an estimated value of

the dipole impedance–accurate enough to serve as a starting point for Pre2amp design–impedance modeling of a dipole in a real environment requires a more exhaustive analysis. This is caused by the capacitive coupling between the antenna and the surrounding environment, whose effect can be modeled as a shunt capacitor with unknown value in Fig. 2.2. Since this value is unknown and heavily dependent on the environment the antenna is placed in, determining a precise and accurate value for the dipole impedance requires real-time measurements of the dynamic environmental conditions in the near-field region of the antenna.

2.1.2 Pre2amp

As shown in Section 2.1.1, the ULNA in Pre2amp should be designed concurrently with the antenna. Hence, for the amplifier design, we need to use the previously calculated antenna parameters. The circuit design of the ULNA is shown in Fig. 2.6. The ULNA is made out of two cascaded stages. The first stage serves as both a buffer and the primary amplification stage, and the second stage provides additional variable gain while increasing the common-mode rejection ratio (CMRR) of the ULNA. The amplifier is powered by a differential supply ($\pm$10.8 V) driven from Preamp. A resistor divider with a buffer is used between the rails to create a virtual ground. Instead of driving a ground cable, a virtual ground is used to keep all signals and power differential, minimizing noise and distortion coupled from external sources. This also eliminates the need for a fifth wire to be driven between Pre2amp and Preamp and enables a compact signal and power transmission with two differential wire pairs. A buffer between the resistor divider and Pre2amp circuitry is needed due to possible loading. The buffer is an op-amp in unity-gain configuration. This op-amp was chosen to be OPA211, a unity-gain stable op-amp with 1.1 $\mathrm{nV}/\sqrt{\mathrm{Hz}}$ RTI voltage noise spectral density.

Since the dipole antenna serves as the interface between the front-end circuitry and the incoming electromagnetic waves, signals coming from the dipole are highly susceptible to

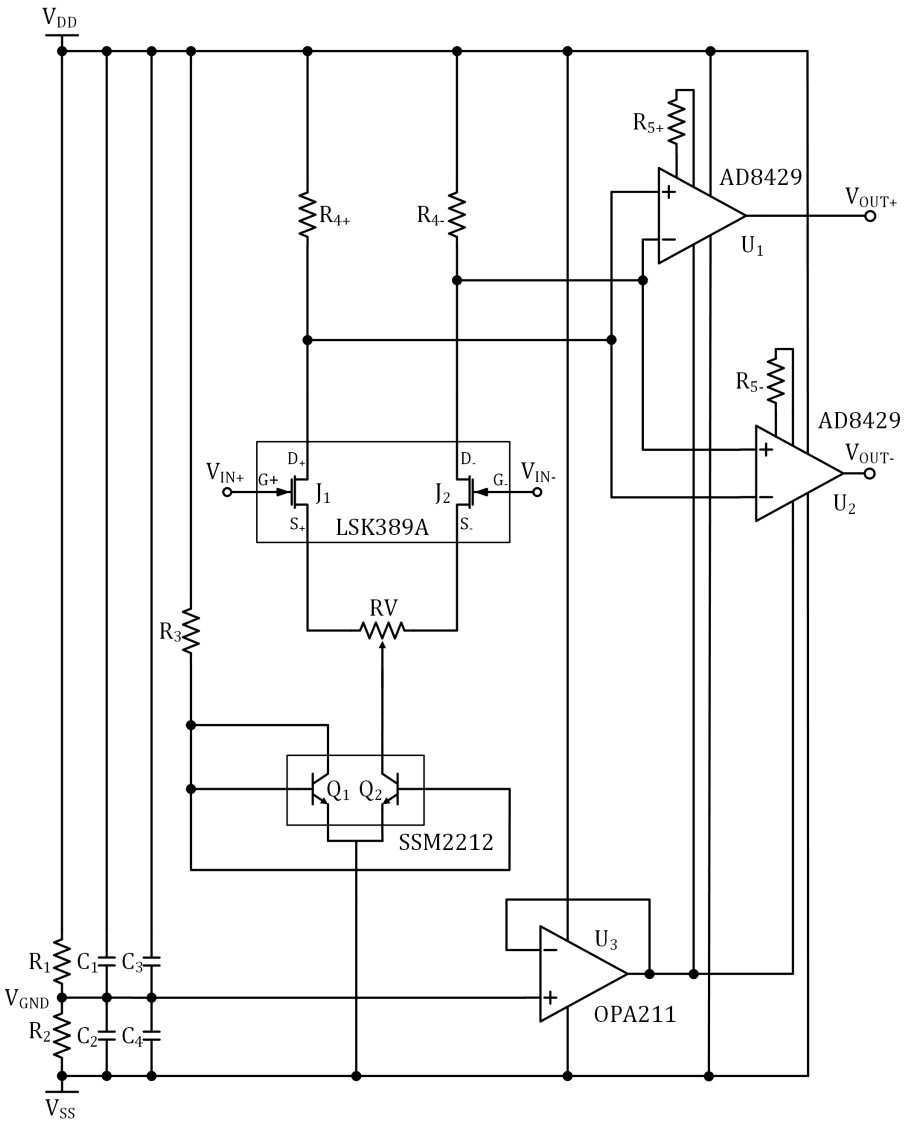

Figure 2.6: Differential ultra-low noise amplifier circuit schematic.

distortion and SNR degradation before they are amplified. Furthermore, any load–a long microstrip line or any cable-between the antenna and the front-end circuitry could result in loss in signal amplitude due to the degradation of efficiency. Therefore, the antenna is directly connected to the inputs of Pre2amp first stage on the same board with traces as short as possible. For the same reason, the design of the first stage is critical for the successful operation of the receiver.

Since the dipole impedance becomes the source impedance for the amplifier's first

Table 2.1: Component list for Pre2amp

Designator	Component Type	Component Value
J_1, J_2	Low-Noise JFET Pair	LSK389A
Q_1, Q_2	Low-Noise BJT Pair	SSM212
U_1, U_2	Instrumentation Amplifier	AD8429
R_1, R_2	Thin film resistor, 0.01%	10 kΩ
R_3	Thin film resistor, 0.1%	4.64 kΩ
R_4	Thin film resistor, 0.1%	2.2 kΩ
R_5	Thin film resistor, 0.1%	DNL, 667, 60.6, 6 Ω
RV	Trimpot, 10%, 12 turns	10 Ω
C_1, C_2	Molded tantalum capacitor, 10%	0.1 μF
C_3, C_4	Molded tantalum capacitor, 10%	10 μF

stage, the first stage needs to be designed according to the source impedance over the operating frequency range. Firstly, as discussed earlier, due to the high source impedance at low frequencies, voltage noise equivalent of the current noise can be significant if the input current noise of the first stage is not minimized. Secondly, input impedance of the first stage and output impedance of the dipole forms a voltage divider. Therefore, magnitude of the transfer function of this voltage divider can be approximated as

$$|T(s)| \approx \sqrt{\frac{R_{in}^2 + X_{in}^2}{R_{in}^2 + (X_a + X_{in})^2}} \tag{2.17}$$

where R_{in} is the input resistance of the first stage and X_{in} is the input reactance of the first stage. For maximum voltage transfer, namely $|T(s)| \approx 1$, the first stage should have a high input resistance and a low input capacitance.

There are various devices that satisfy either or both of these requirements. Due to their low input resistance and high noise, BJTs are not suitable for the first stage. FETs, on the other hand, have high input resistance and low noise. More specifically, JFETs have the lowest flicker noise and offer high gain, making them advantageous to be used in the first stage.

There are various off-the-shelf discrete JFETs that offer low RTI (referred-to-input) voltage and current noise. While current noise is the most important factor in choosing

the right JFET, LSK389A from Linear Systems is a JFET pair that has an RTI voltage noise spectral density of $1.3\ \mathrm{nV}/\sqrt{\mathrm{Hz}}$ at 1 kHz, an input resistance of $1\ \mathrm{T}\Omega$, and an input capacitance of 22 pF. This JFET pair is used as a common-source amplifier in the first stage. The connection between the first stage and the dipole should also be designed carefully. Since any cable or connector would add significant input capacitance, the dipole is directly soldered onto pads on Pre2amp, which are connected to first-stage inputs. Traces from these pads to the ULNA are kept as short as possible to minimize parasitic capacitance from the traces (0.05 pF per 1 mm for a standard PCB). Shunt resistors at the inputs of the first stage in order to create a return path for the input bias currents are also not necessary due to the extremely-small input bias currents of LSK389A. This is beneficial as any resistor at the input would add significant thermal noise to the receiver.

In order to minimize the noise contributions of subsequent stages, the first stage voltage gain is maximized while maintaining linearity. To achieve this, the gain is usually set so that the amplified signal is within the dynamic range of the back-end analog-to-digital converter (ADC). However, in this design, the gain is set so that the input signal is amplified beyond the ADC clipping voltage. Then, the signal is attenuated in Preamp before driving the signal to the ADC to prevent the ADC from being saturated. This is required due to the extremely low sensitivity of the receiver as even the smallest noise from subsequent stages will have substantial effect on the overall sensitivity. Therefore, the first stage gain is maximized at 36 dB so that the amplified signal is at the ceiling of the first stage dynamic range, which is 6.8 V. This puts the maximum input voltage the first stage can amplify at 0.1 V.

LSK389A is a tightly-matched pair with a differential gate-to-source cut-off voltage, $|\mathrm{V_{GS1}} - \mathrm{V_{GS2}}|$, of 6 mV. However, with a gain of 36 dB, this voltage difference adds an offset to the output of around 0.4 V. This offset could be significant especially when the input differential signal is large since this offset might clip one of the output lines. In order to mitigate this, a variable resistor of 10 Ω, RV, is added at the source of the JFET. The resistance of RV is tuned until $|\mathrm{V_{GS1}} - \mathrm{V_{GS2}}|$ is 0, eliminating any DC offset at the output.

Lastly, the bias current for the first stage is supplied by a low-noise BJT pair, SSM2212, in current mirror configuration. The current mirror supplies 4 mA current to the first stage.

The second stage is comprised of two instrumentation amplifiers, AD8429, with an RTI voltage noise spectral density of 1 $\mathrm{nV}/\sqrt{\mathrm{Hz}}$ and an RTO (referred-to-output) voltage noise spectral density of 45 $\mathrm{nV}/\sqrt{\mathrm{Hz}}$. Differential input instrumentation amplifiers are used in order to improve the CMRR of the ULNA and increase the dynamic range by driving two outputs from the first stage into two differential input pairs in the second stage. There is, again, no need for shunt resistors to create a return path for input bias currents as the input bias current (150 nA) for the second stage is within the range of output current that can be supplied by the first stage.

Furthermore, the second stage provides additional variable gain to the ULNA. The variable gain of the instrumentation amplifiers is between 0 dB and 80 dB, which is set by R_6. Overall, with the first stage, ULNA has four gain configurations: 42 dB, 62 dB, 82 dB, or 102 dB. These gains are set when R_5 is open, 667 Ω, 60.6 Ω, and 6 Ω respectively. The nominal bandwidth of the ULNA is 2.2 MHz (6 Hz-2.2 MHz), enabling broadband radio reception. However, the highest gain setting caps the bandwidth at 150 kHz, therefore, should only be used when ELF/VLF signal detection is desired. Lastly, the maximum input signal amplitude that is within the dynamic range of the ULNA is 100 mV.

The second stage also drives the signal through the potentially long cable between Pre2amp and Preamp. This cable is a shielded Cat5e Ethernet cable with 52 pF/m capacitance. With 10,000 pF capacitive load driving capability, the ULNA can drive any Cat5e Ethernet cable shorter than 192 m, enabling great flexibility in the placement of Pre2amp and dipole.

Selection of the parts is also important in such a low-noise circuit as various types of discrete components add different levels of noise to the system. The components used in Pre2amp and their types are shown in Table 2.1. Resistors have two uncorrelated noise components: Thermal noise and excess noise. Thermal noise is independent of the compo-

nent type and is a characteristic of the resistance value. In order to minimize thermal noise, resistor values ought to be minimized without adding distortion to the system or compromising the system stability. Excess noise depends on the material the resistor is made out of and the manufacturing process. Out of all resistor types, discrete wirewound resistors have the lowest excess noise; however, they usually have inductive elements associated with them, allowing external parasitics to be coupled into the circuit. Integrated thin film resistors have slightly higher excess noise, but they do not have any inductive effects and are more convenient to use due to their small size.[30]

Capacitors also have thermal and excess noise. Thermal noise manifests itself due to the series and leakage resistances non-ideal capacitors have but is negligible since this resistance is usually on the order of a few Ωs. Excess noise is also negligible but might be present in electrolytic capacitors after they are exposed to reverse bias conditions. Ceramic capacitors have piezoelectric effects, which couple into the circuit as voltage noise. Both film and electrolytic capacitors have comparable noise, but molded tantalum electrolytic capacitors, specifically, have the lowest thermal noise and virtually no excess noise if necessary precautions are taken so that they are never reverse biased.

With these considerations, we can create a noise model of the entire system by focusing on the noise contribution of just Pre2amp. The noise model of the system can be reduced to the noise model of the ULNA in Pre2amp since the noise contributions of the subsequent stages after Pre2amp is negligible due to Pre2amp's high gain. We also neglect any noise contribution from the discrete capacitor and excess noise from the discrete resistor components assuming the necessary precautions specified above are taken to minimize their parasitic behavior. Therefore, the noise model of Pre2amp is shown in Fig. 2.7.

In this model, a few assumptions are made to simplify the calculations while not maintaining its accuracy. Since this system is intended to be used at low frequencies, any reactive components that would be included in a high-frequency model are neglected from this model. Furthermore, due to the high output conductance of BJTs and JFETs used in

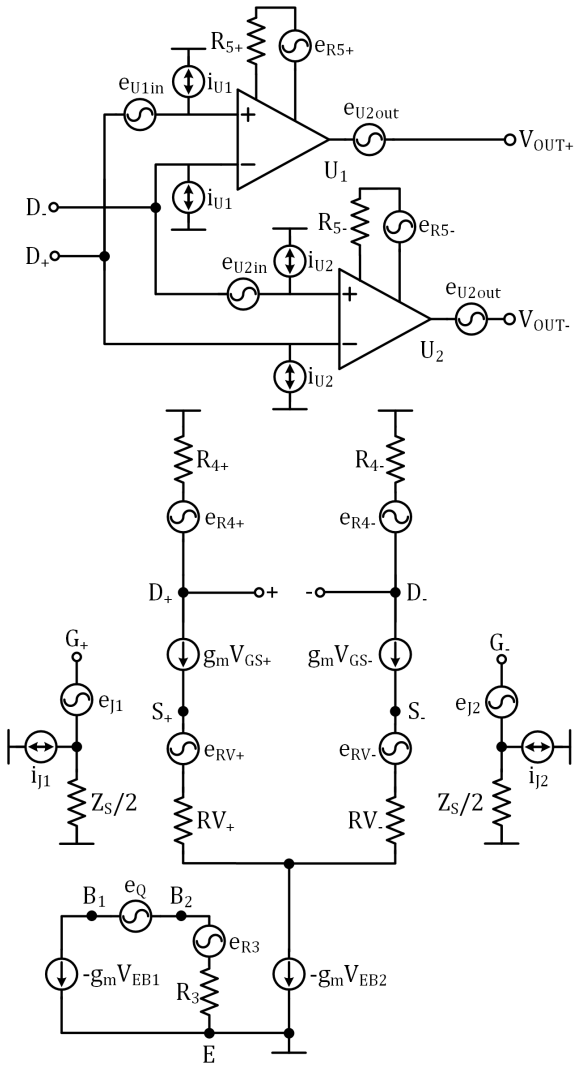

Figure 2.7: Circuit model of the ULNA for noise calculations.

Pre2amp, output resistances are also neglected from the model. Calculating the RTI noise spectral density, all noise sources are assumed to be uncorrelated. Therefore, we can consider the noise contribution of each noise source at the output of its corresponding stage independently and divide the output voltage noise by the gain of the prior stages to obtain its contribution to the input noise. Then, we can use superposition to determine the RTI noise spectral density.

To begin with, we need to consider the noise contribution of the current mirror. As seen in Fig. 2.7, input voltage noise of the BJTs , e_Q, and thermal noise of the current-setting

resistor, e_{R3}, do not directly contribute to the RTI voltage noise but manifest themselves as current noise in $i_Q = -g_m V_{EB2}$. Consequently, this current noise sets the source voltage of both JFETs as $S = \frac{i_Q RV}{2}$. Thus, the input voltage noise due to i_Q is calculated as

$$e_{iQ}^{in} = e_1 = \frac{g_m i_Q RV R_4}{2G_1} \tag{2.18}$$

where G_1 is the voltage gain of the first stage, which is 36 dB as mentioned in Section 2.1.2. Using superposition, we can also derive i_Q,

$$i_Q = \frac{g_m^2 e_Q R_3}{g_m R_3 + 1} + \frac{g_m e_{R3}}{g_m R_3 + 1} = \frac{g_m \sqrt{g_m^2 e_Q^2 R_3^2 + 4k_B T R_3}}{g_m R_3 + 1} \tag{2.19}$$

We now consider the thermal noise of RV, e_{RV}. The input voltage noise due to e_{RV} is calculated as

$$e_{RV}^{in} = e_2 = \frac{g_m e_{RV} R_4}{G_1} = \frac{2g_m R_4 \sqrt{k_B T RV}}{G_1} \tag{2.20}$$

Then, we consider the thermal noise of R_4, e_{R4}. The input voltage noise due to e_{R4} is calculated as

$$e_{R4}^{in} = e_3 = \frac{e_{R4}}{G_1} = \frac{2\sqrt{k_B T R_4}}{G_1} \tag{2.21}$$

The input voltage noise due to the input current noise of the first-stage JFETs depend on the source impedance, which is the impedance of the dipole antenna. Therefore, this noise is highly variable with frequency as shown in Section 2.1.1. The input voltage noise due to i_J is calculated as

$$e_{iJ}^{in} = e_4 = i_J \frac{Z_S}{2} \tag{2.22}$$

where Z_s is the dipole impedance. Since the input voltage noise contribution of the input voltage noise of the JFETs, e_J, is $e_5 = e_J$, we can move on to the second stage. The input voltage noise due to the input voltage noise of the instrumentation amplifiers, e_{Uin}, is

calculated as

$$e_{Uin}^{in} = e_6 = \frac{e_{Uin}}{G_1} \tag{2.23}$$

Calculating the input voltage noise due to the input current noise of the instrumentation amplifiers, i_U, we need to add all current noise contributions using superposition. Therefore,

$$e_{iU}^{in} = e_7 = \frac{1}{G_1}\sqrt{2\left(i_U\frac{Z_{out1}}{2}\right)^2} = \frac{i_U Z_{out1}}{G_1\sqrt{2}} \tag{2.24}$$

where Z_{out1} is the output impedance of the first stage, which is calculated as $Z_{out1} = \frac{R_4}{g_m R_4+1}$. The input voltage noise due to the thermal noise of R_5, e_{R5}, is calculated as

$$e_{R5}^{in} = e_8 = \frac{e_{R5}}{G_1} = \frac{2\sqrt{k_B T R_5}}{G_1} \tag{2.25}$$

Lastly, the input voltage noise due to the output voltage noise of the instrumentation amplifies, e_{Uout}, is calculated as

$$e_{Uout}^{in} = e_9 = \frac{e_{Uout}}{G_1 G_2} \tag{2.26}$$

where G_2 is the voltage gain of the second stage, characterized by $G_2 = 1+\frac{6000}{R_4}$. Therefore, using superposition, the overall RTI noise spectral density can be calculated as

$$e_n^{in} = \sqrt{2\sum_{i=1}^{9} e_i^2} \tag{2.27}$$

All of the noise contributions due to thermodynamic effects are additive additive white Gaussian noise, meaning their spectral densities are frequency invariant. Since g_m is also frequency invariant within the operation conditions of the system, e_2, e_3, and e_8 can be assumed constant over the frequency spectrum the system is operating in. On other hand, noise contributions due to the intrinsic noise of the transistors and amplifiers are frequency variant. The most significant cause to this frequency variance comes from the flicker noise of these solid-state devices. Therefore, the corner frequencies of these devices for their

flicker noise is important to specify. The corner frequency of the voltage flicker noise of SSM2212 and AD8429 are on the order of 1 Hz and 10 Hz respectively, whereas the corner frequency of the current flicker noise of AD8429 and the voltage flicker noise of LSK389A are on the order of 100 Hz and 10 kHz respectively. Furthermore, although the current noise of LSK389A might be frequency variant, its voltage noise contribution that heavily depends on the dipole impedance is not. Therefore, we can assume e_1, e_6, and e_9 to be constant over the frequency spectrum. However, to accurately characterize the noise contributions of the current noise of AD8429, the voltage and the current noise of LSK389A, we need to plot e_4, e_5 and e_7 with respect to frequency. The overall RTI voltage noise spectral density of the ULNA and the voltage noise contributions of the aforementioned noise sources are shown in Fig. 2.8.

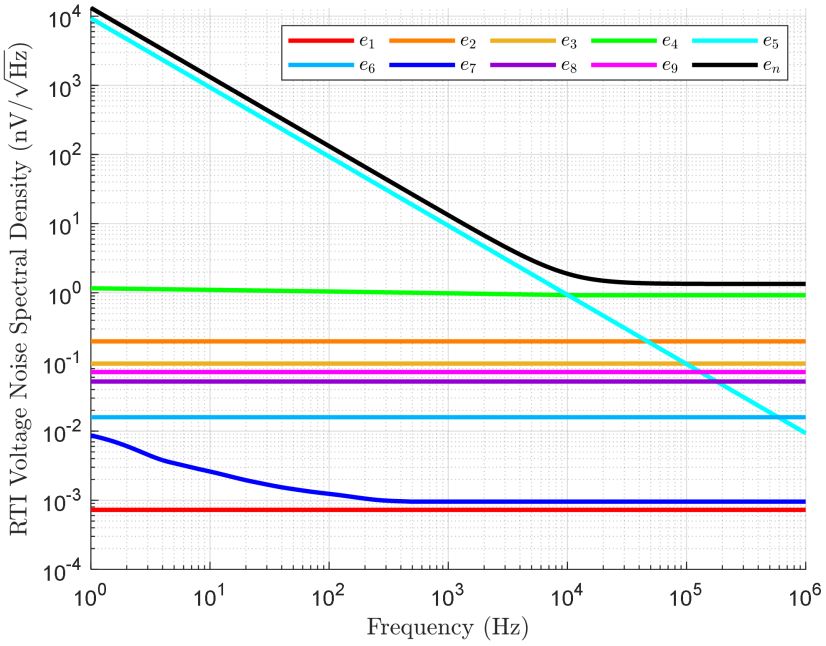

Figure 2.8: Modeled RTI voltage noise spectral density of the ULNA and the voltage noise contributions of all the noise sources.

As seen in Fig. 2.8, the overal RTI voltage noise is dominated by e_4 at high frequencies, and by e_5 at low frequencies. This cements the argument that the input current noise of the first stage needs to be as small as possible to drive the corner frequency where e_4 starts

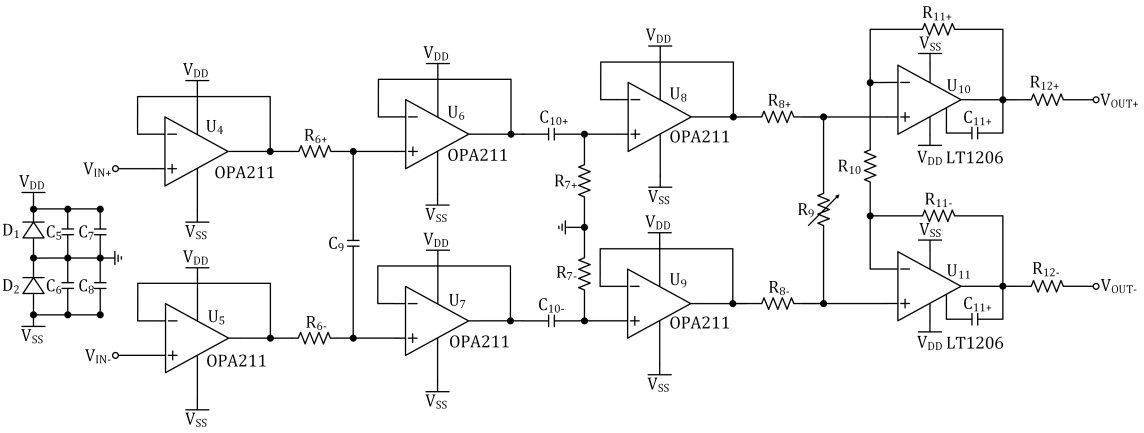

Figure 2.9: Preamp circuit schematic when all filters are enabled.

to dominate as low as possible. Furthermore, the input voltage noise of the first stage is critical to make the overall RTI voltage noise as small as possible.

2.1.3 Preamp

Table 2.2: Component list for Preamp

Designator	Component Type	Component Value
U_{3-8}	Low-Noise Op-Amp	OPA211
U_9, U_{10}	Low-Noise Amplifier	LT1206
D_1, D_2	Semiconductor Diode, 100 V	1N914
R_6	Thin film resistor, 0.1%	318 Ω
R_7	Thin film resistor, 0.1%	1.59 kΩ
R_8	Thin film resistor, 0.1%	164 Ω
R_9	Trimpot, 10%, 25 turns	500 Ω
R_{10}, R_{11}	Thin film resistor, 0.1%	1k Ω
C_5, C_6	Molded tantalum capacitor, 10%	0.1 μF
C_7, C_8	Molded tantalum capacitor, 10%	10 μF
C_9	Molded tantalum capacitor, 10%	500 pF
C_{10}	Molded tantalum capacitor, 10%	0.1 μF

Preamp serves multiple purposes and is comprised of five cascaded stages. Preamp circuit design is shown in Fig. 2.9. Preamp is separated from Pre2amp because Preamp enables this receiver to be integrated with a magnetic field receiver similar to the one proposed in [18] for simultaneous electric and magnetic field reception. Preamp combines one

electric-field channel with two magnetic-field channels coming from two orthogonal loop antennas to enable a hybrid electric and magnetic field receiver. After they are combined, these channels are driven to the back end.

First stage of Preamp is a buffer stage to receive the signal driven from Pre2amp. It uses OPA211 in unity-gain configuration.

Second and third stages are passive differential low and high-pass filters with op-amp buffers in between them. Low-pass filter has a cut-off frequency of 500 kHz, and high-pass filter has a cut-off frequency of 1 kHz. These filters are necessary as there are significant external noise sources whose signals can couple into the receiver as voltage and current noise. At high frequencies, AM radio transmissions (535-1705 kHz) dominate the external noise environment and are filtered out by the low-pass filter. At low frequencies, 60 Hz emissions and their harmonics from power lines dominate and are filtered out by the high-pass filter. However, there are cases—for instance, when these sources are intended to be observed or at remote locations where noise from power lines and AM transmissions is weak—for which disabling either or both of these filters is beneficial. Therefore, Preamp also has jumper connectors which, if shorted, disable either or both of the filters, enabling manual reconfigurability.

Passive filters are used instead of active op-amp filters with reactive feedback due to their superior RTI noise. Modeling the RTI noise of a first-order passive filter and a first-order active filter with the same cut-off frequency (same RC) as shown in Fig. 2.10, there are two uncorrelated voltage noise sources equal in spectral density, $e_n = \sqrt{4k_BTR}$. Using superposition, we can find the RTO voltage noise spectral densities of both passive and active filters in the passband region. For active filters in Fig. 2.10 (left), $e_{out} = \sqrt{e_n^2 \left(\frac{R}{R}\right)^2 + e_n^2} = e_n\sqrt{2}$. For passive filters in Fig. 2.10 (right), $e_{out} = e_n$. Therefore, active filters have $\sqrt{2}$ times the RTO noise as passive filters, making the use of passive filters in Preamp more beneficial. This passive filter configuration also has the added benefit of having fewer components, driving down the cost.

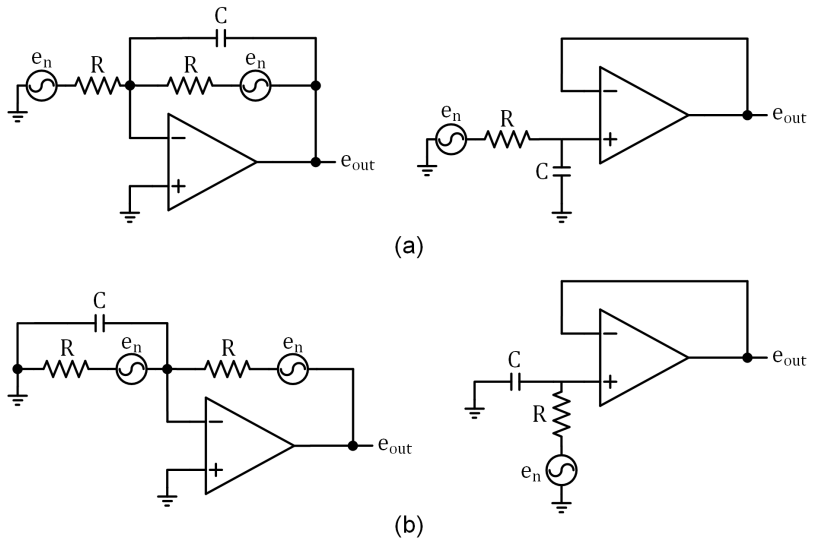

Figure 2.10: Noise models of active and passive first-order (a) low-pass filters (b) high-pass filters

Fourth stage is a passive attenuator reconfigurable via a shunt variable resistor. This attenuation at the end of the front-end before driving the signal to the back-end is needed to attenuate the high-amplitude signal amplified at Pre2amp and prevent clipping at the back-end. The attenuator is made reconfigurable to allow for greater flexibility in the ULNA design process in Pre2amp. However, for this ULNA design, the nominal attenuation is set to be -2.19 dB, bringing down the overall gain of the receiver to 40 dB, 60 dB, 80 dB or 100 dB. These gains are named low gain, medium gain, high gain, and very high gain, respectively.

Fifth stage is an op-amp driver, which drives the signal from the front end to the back end. LT1206 is a low-noise current feedback amplifier with an RTI voltage noise density of 3.6 $\mathrm{nV}/\sqrt{\mathrm{Hz}}$ at 1 kHz. It is capable of driving loads up to 20,000 pF, allowing the front-end to be separated from the back-end by the Belden 1217B audio cable as long as 321 m. This separation is crucial since any digital back end circuitry can couple into the front end as an external noise source.

Selection of the parts used in Preamp follow the same design guidelines outlined in Section 2.1.2. These components and their types are shown in Table 2.2.

After Preamp, signals detected by the electric field receiver can be multiplexed with the signals detected by a magnetic field receiver, such as the AWESOME receiver. In the case of the AWESOME receiver, two channels–due to two loop antennas–are needed to drive the detected signals to the back-end. A chassis fitted with a backplane board is used to multiplex two channels from the magnetic field receiver with one channel from this electric field receiver. The backplane hosts edge connectors to which Preamp and magnetic field receiver preamplifier cards can be connected to. The backplane also serves as the interface between Preamp and the audio cable the system uses to drive the signals and power between the front-end and the back-end. Three differential wire pairs of this cable are used to carry the signals from the front-end to the back-end and the fourth pair is used to carry power from the back-end to the front-end.

2.1.4 Data Processing and Storage

The back-end is responsible for providing power to the system, data processing and storage after the signals are driven from the front-end to the back-end. The back-end is comprised of two components, line receiver and a data storage unit. The architecture and performance of the line receiver are discussed in [18] and will be briefly reviewed here.

The line receiver rejects common-mode interference coupled into the differential signals driven to the back-end, performs anti-aliasing filtering, GPS time-stamping and synchronization, and digitizes the analog signals with an integrated ADC. The line receiver also provides power to the entire system.

After the differential signals are converted into single-ended signals through the instrumentation amplifier, they are passed onto the anti-aliasing filter. This filter is comprised of three cascaded low-pass filters with a low-pass cut-off at 470 kHz. The anti-aliasing filter can be reconfigured to operate as an 8th order or 12th order elliptical low-pass filter.

The custom ADC, made by National Instruments, provides 16 bit (96 dB) dynamic range at a 1 MHz sampling rate for signal digitization. 1 MHz sampling clock is generated

by a voltage-controlled oscillator synchronized to a GPS receiver. This GPS synchronization circuitry generates a synchronized sampling clock accurate to an RMS of 15 nS. This timing accuracy is made possible by an error correction algorithm implemented with a microcontroller, which phase locks the 40 MHz VCO to a 1 pulse-per-second (PPS) GPS receiver.

After the signals are digitized through the ADC, they are driven and stored in the computer, which also hosts a custom data-acquisition software. This software enables various data recording modes for different applications as described in [19]. After being stored on the local drive, recorded LF data are acquired and made publicly available through the WALDO initiative discussed in [31].

2.2 Calibration

Calibration process encompasses characterizing the frequency response of the system. For magnetic field receivers, this process entails injecting a single-frequency current signal with known amplitude and phase into the input of the receiver and measuring the amplitude and phase at the receiver output over the entire operating frequency range. For magnetic field receivers with air-core loops, the injected current signal can be analytically matched to its corresponding magnetic flux density due to the electromagnetic model of the loop antenna's accordance with the Faraday's law and due to the lack of significant coupling between the loop and the surrounding environment. Due to this predictability of the loop antenna's electromagnetic behavior, calibration of a magnetic field receiver is rather straightforward.

On the other hand, calibration of an electric field receiver is an arduous task due to capacitive coupling of an electric field antenna with the surrounding environment, whose effect on the circuit model is discussed in Section 2.1.1. Due to capacitive coupling, the frequency response of the antenna-amplifier changes based on the environment the receiver is placed in and its dynamic conditions. Consequently, this makes the method of matching the injected signal to its corresponding electric field value imprecise. Since our electric

field receiver will be deployed in a wide selection of dynamic environments, another calibration method is needed to precisely and accurately calibrate the system. We propose and demonstrate two calibration methods through which any electric field receiver could be calibrated.

2.2.1 Direct Calibration

The so-called direct calibration method builds upon the calibration method of a magnetic field receiver using air-core loops. This requires the electric field receiver to be placed in an electric field cage, in which the receiver is isolated and shielded from the outside environment. In the cage, the receiver is exposed to a uniform, single-frequency electric field plane wave with known amplitude and phase. As the plane wave is picked up by the receiver, the amplitude and phase of the receiver output is recorded and compared with the amplitude of the detected electric field to obtain the gain and phase shift of the system at that frequency. This process is then repeated over the entire operating frequency range to obtain the frequency response of the system.

We utilized such a cage in the US Army Research Laboratory (ARL) in Adelphi, MD. The cage is essentially a parallel-plate capacitor with two endplates. The antenna was placed in the middle of this 2.4 m high by 3 m wide by 4.2 m long (in the field direction) and was exposed to a uniform electric field [32]. Due to the height limitation, the receiver could only be calibrated for 1 m and 2 m dipole antennas. A frequency sweep of the receiver response for all four gain configurations was performed. Furthermore, due to the different clipping thresholds of the system based on the gain configuration, amplitude of the uniform electric field the receiver is exposed to was set close to but below the clipping threshold of each configuration. The amplitudes were set close to the clipping thresholds to minimize any parasitic effect a noise source could have in the calibration process.

2.2.2 Indirect Calibration

The so-called indirect calibration method takes advantage of the straightforward calibration process of a magnetic field receiver and the nature of electromagnetic wave propagation in the far-field region of a source. This method involves using both this electric field receiver and a magnetic field receiver simultaneously. From the magnetic field receiver, a sferic waveform needs to be identified that satisfies three conditions:

1. The source of the sferic needs to be far away enough from the receiver so that the receiver is in the far-field region of the source. This is required so that the electric and magnetic fields can be assumed to be in-phase and the electric-to-magnetic field (E-to-B field) amplitude ratio can be approximated as $1/\sqrt{\mu\epsilon}$, where μ and ϵ are the permeability and permittivity of air respectively.

2. In the frequency domain, the sferic waveform magnitude needs to be above the noise floor of the receiver for every frequency that is in the operating frequency range of the receiver.

3. If the measurement was taken during the day, the entire sferic propagation path needs to in daytime, and if it was taken during the night, the propagation path needs to be in nighttime. Usually, this condition can be satisfied by finding a sferic with a source at around the same longitude of the detection location.

While the first two conditions are more easily understood, third condition requires more in-depth explanation. Due to greater solar activity during daytime, ionosphere becomes more ionized, causing the lowest layer of the ionosphere, the D layer, to form at an altitude of around 60 km. On the other hand, during nighttime, reduced solar activity causes the D layer to disappear, leaving the one upper layer, the E layer, to be the lowest layer of the ionosphere at an altitude of around 90 km. This leads to a discontinuity in this ionization altitude at the transition between daytime and nighttime regions of the Earth. This discontinuity acts as a scatterer to any LF waves that interact with it. This scattering then alters the

waveform characteristics, invalidating the in-phase electric and magnetic fields assumption and E-to-B field amplitude ratio approximation.

After such a sferic magnetic field waveform is identified in the magnetic field data, its corresponding electric field waveform needs to be also identified in the electric field data. Since the magnetic field receiver can be calibrated relatively easily as discussed earlier, the calibrated (absolute) magnetic field phasors of the waveform are calculated in the frequency domain. Assuming the E-to-B field amplitude ratio is $1/\sqrt{\mu\epsilon}$ and both fields are in-phase, these phasors are multiplied by $\sqrt{\mu\epsilon}\angle 0^\circ$ to obtain their corresponding absolute electric field phasors. Then, it is assumed that the detected electric field phasors in the frequency domain also correspond to the absolute electric field phasors. Therefore, the ratio of the absolute amplitude to the detected amplitude gives the gain and the phase difference between the absolute phase and detected phase gives the phase shift of the electric field receiver at that frequency.

While this method provides a practical way to calibrate the electric field receiver relatively accurately, it has some shortcomings that are worthwhile to be addressed. Primary shortcoming stems from the assumption that the identified sferic satisfies the propagation conditions in a far-field region. Since the validity of the calibration process is dependant on this assumption, any deviation from this condition in the real propagation of the sferic affects the accuracy of the acquired amplitude response. Especially considering how the sky-wave propagation of sferics can be affected in the EIW as they interact with lower layers of the ionosphere, there are numerous situations where this assumption can fall short even if the aforementioned three conditions are met.

Therefore, we advise the indirect method to be used when a quick calibration of the receiver is needed, such as during a deployment at a remote site. However, in other instances where a more accurate amplitude response of the receiver is needed, the direct method should be used.

CHAPTER 3

RESULTS

3.1 Receiver Performance

We now present the empirical data obtained in characterizing the receiver and an analysis of the real-time broadband data from one of the deployed electric field receivers.

3.1.1 Frequency Response

The receiver's frequency response with 1 m and 2 m dipole antennas obtained via the aforementioned indirect calibration process is shown in Fig. 3.1.

The frequency response above 80 kHz was not obtained since the sferics used in the calibration process did not have a magnitude above the noise floor above this frequency. However, it is observed that the receiver has a relatively flat amplitude response above 1 kHz with the antenna length serving as a scaling factor to the gain. The drop-off at 1 kHz can be attributed to the high-pass filter in Preamp and can be removed by simply disabling the filter. The phase response is not affected by the antenna length and is noisy. This erratic behavior most likely results from the undesired circumstances in the sferic propagation environment, since the in-phase electric and mangetic field condition is harder to satisfy in the EIW than unity E-to-B-field amplitude ratio. As briefly discussed in Section 2.2.1, receiver gain also sets the maximum electric field amplitude the receiver can detect before it clips. Higher gain corresponds to lower clipping threshold and vice versa. Clipping thresholds calculated from the receiver gain data along with previously detailed information about each configuration are shown in Table 3.1.

Due to the dependence of the clipping threshold on the receiver gain, the gain configuration should be chosen based on the environment (i.e. intensity of the signals that are of

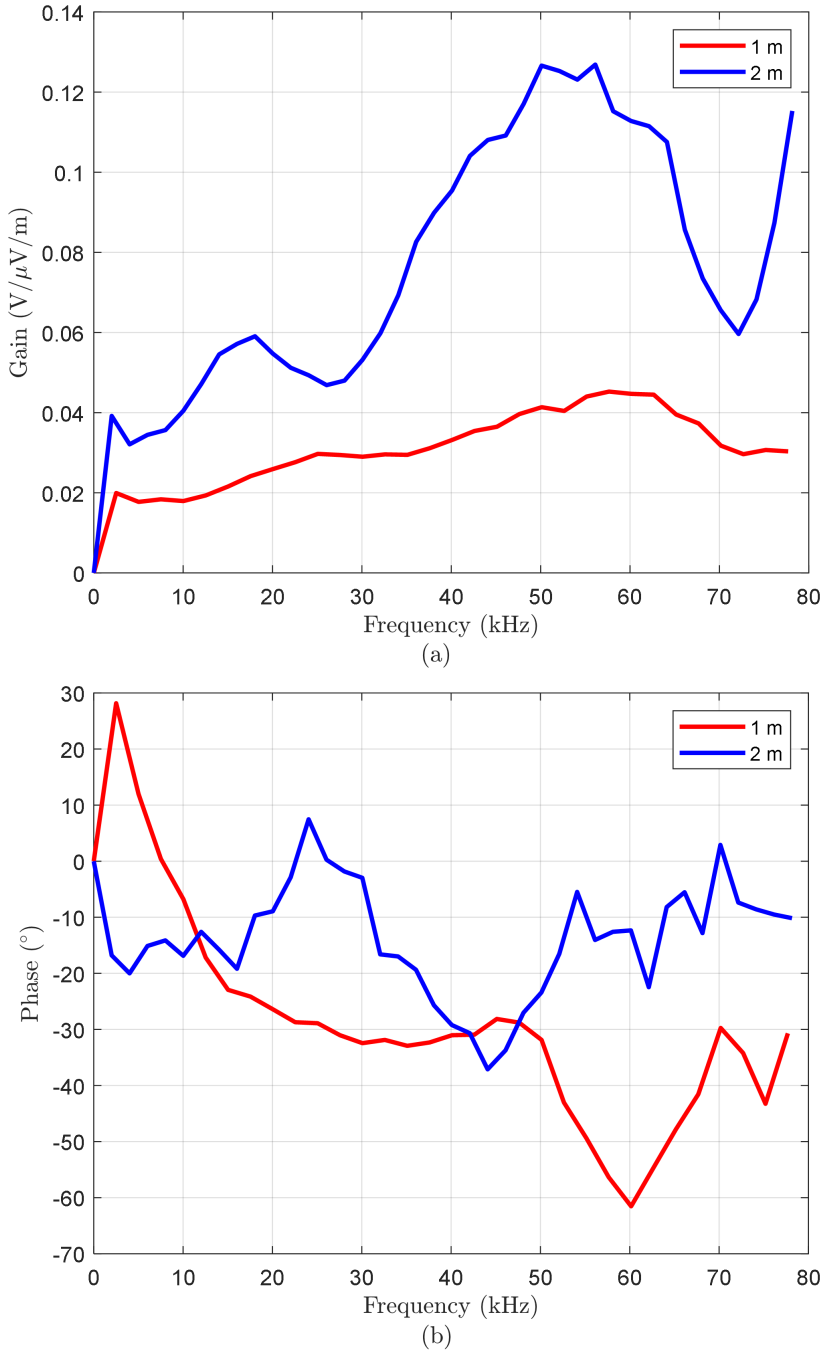

Figure 3.1: Frequency response of the receiver obtained via the indirect calibration method. a) Amplitude response. b) Phase response.

interest) where the receiver is deployed. In our experience, in an urban setting where the signals of interest are sferics and narrowband signals from man-made transmitters, medium gain configuration is the most suitable because of potential clipping due to power line noise.

Table 3.1: Gain configuration summary

Configuration Name	Dipole Length	Front-End Gain	Threshold
Low Gain	1 m	40 dB	25 mV/m
	2 m	40 dB	12.5 mV/m
Medium Gain	1 m	60 dB	2.5 mV/m
	2 m	60 dB	1.25 mV/m
High Gain	1 m	80 dB	0.25 mV/m
	2 m	80 dB	0.125 mV/m
Very High Gain	1 m	100 dB	0.025 mV/m
	2 m	100 dB	0.0125 mV/m

On the other hand, in a rural setting–away from power line and other man-made noise–high gain configuration is the most suitable.

3.1.2 Sensitivity

After the calibration, the sensitivity of the receiver can be characterized by simply disconnecting the antenna and measuring the output without any electrically induced voltage at the receiver inputs. To further minimize the intensity of external signals coupling into the receiver circuitry, the receiver is placed in a metal container for shielding.

After the experimental setup is assembled, the output is measured and gets divided by the frequency response obtained from the calibration to calculate the electric field equivalent of the output noise. This result becomes the sensitivity of the receiver. Hence, the sensitivity of the receiver at high gain configuration calibrated for both 1 m and 2 m dipole antennas via indirect calibration is shown in Fig. 3.2.

As seen in Fig. 3.2, the receiver sensitivity stays below 30 $\mathrm{nV}/(\mathrm{m}\sqrt{\mathrm{Hz}})$, or 0.1 $\mathrm{fT}/\sqrt{\mathrm{Hz}}$, across the entire spectrum and reaches a minimum sensitivity of 0.17 $\mathrm{nV}/(\mathrm{m}\sqrt{\mathrm{Hz}})$, or 0.57 $\mathrm{aT}/\sqrt{\mathrm{Hz}}$, at 54 kHz. This result can also be used to compare this electric field receiver with another state-of-the-art receiver. The gray curve above the electric field receiver sensitivity is the characterized sensitivity of the AWESOME magnetic field receiver described in [18]. It stays below 1 $\mathrm{fT}/\sqrt{\mathrm{Hz}}$ across the spectrum and reaches a minimum sensitivity of 0.035 $\mathrm{fT}/\sqrt{\mathrm{Hz}}$ around 35 kHz. Therefore, the minimum sensitivity of the electric field receiver

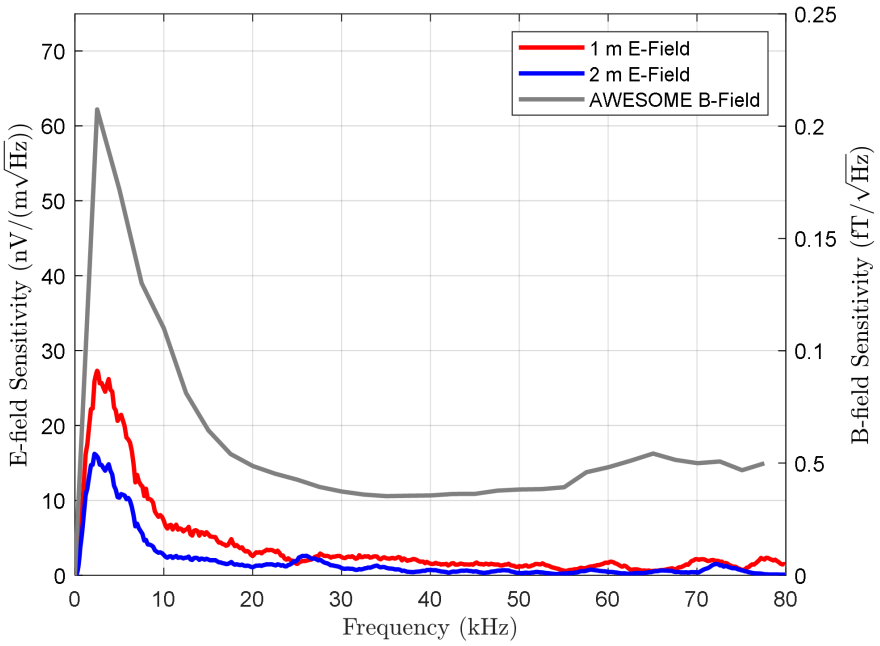

Figure 3.2: Sensitivity of the electric field receiver for different antenna lengths.

is around 34 dB lower than the state-of-the-art, ensuring an improvement in hardware performance of any LF receiver network that utilizes this receiver.

CHAPTER 4
CONCLUSION

In this thesis, we have described a novel instrument that is capable of electric field detection in ELF/VLF/LF/MF bands with unprecedentedly low sensitivity for applications in atmospheric remote sensing, lightning geolocation, imaging through conductive media, and near-field characterization of lightning. Ultra-sensitive instruments serve a key role in radio science since the data analysis starts with these receivers. While magnetic field receivers are conventionally used to detect signals at low frequencies, electric field receivers hold great promise to improve the hardware performance of LF receiver networks and enable novel applications through simultaneous electric and magnetic field detection.

We have detailed the theoretical models for determining the gain and sensitivity of both electric and magnetic field antennas. We have derived closed-form expressions for the sensitivities of both types of antennas in terms of their size and mass as these parameters are crucial to determine the feasibility of a receiver deployment. We have shown the extent of which an electric field antenna with a certain size and mass have lower, namely better, sensitivity than a magnetic field antenna with the same size and mass. We have also outlined two numerical methods for estimating the input resistance and reactance of a dipole antenna, given the significance of estimating these values in the antenna-amplifier co-design.

We have described the circuit architecture, components, and design methodology of the Pre2amp design. We have explained the working principle of the ULNA in Pre2amp along with a summary of its gain configurations. We have outlined the decisions taken in the ULNA design and its design trade-offs. We have presented the noise model of the ULNA and calculated the RTI noise contributions of each noise source to determine the dominating component across different frequency spectra.

We have described the Preamp design–including its working principle, design method-

ology, and design trade-offs. In this description, we have also shown the high-level architecture with which this electric field receiver can be integrated with two channels of data from a magnetic field receiver.

We have summarized the working principle of the back-end in which the detected signals are processed and stored.

Fifth, we have proposed and demonstrated two novel calibration methods to characterize the frequency response of any electric field receiver operating at low frequencies with adequate accuracy.

Lastly, we have shown the amplitude and phase responses obtained via the proposed indirect calibration method along with the sensitivity of the electric field receiver between 0-80 kHz. Through these results, we have shown that the electric field receiver achieves $\sim$34 dB improvement in sensitivity compared to the state-of-the-art, enabling unprecedentedly sensitive signal detection and simultaneous electric and magnetic field detection in LF receiver networks.

REFERENCES

[1] R. Helliwell, *Whistlers and Related Ionospheric Phenomena*. Dover Publications, 2014.

[2] C. J. P. Cave and E. A. W. Watt, "The study of radiotelegraphic atmospherics in relation to meteorology," *Quarterly Journal of the Royal Meteorological Society*, vol. 49, no. 205, pp. 35–39, 1923.

[3] S. Hong and J. King, *Wireless: From Marconi's Black Box to the Audion*. MIT Press, Jan. 2003, vol. 71, pp. 286–288.

[4] G. Marconi, "Guglielmo Marconi - Nobel Lecture," *Nobel Lectures*, 1909.

[5] C. Powell, "Early history of the decca navigator system," *Journal of the Institution of Electronic and Radio Engineers*, vol. 55, no. 6, pp. 203–209, 1985.

[6] K. M. Banks, "Datatrak automatic vehicle location and position reporting system," in *Conference Record of papers presented at the First Vehicle Navigation and Information Systems Conference (VNIS '89)*, 1989, pp. 214–218.

[7] U. S. C. Guard, *Loran-C User Handbook*, ser. CG-462. Department of Transportation, Coast Guard, 1974.

[8] E. R. Swanson, "Omega," *Proceedings of the IEEE*, vol. 71, no. 10, pp. 1140–1155, 1983.

[9] Department of Transportation, *The Nationwide Differential Global Positioning System and Additional Civilian GPS Signals*, 1999.

[10] P. Hansen, "High power very low frequency/low frequency transmitting antennas," in *IEEE Conference on Military Communications*, 1990, 1091–1096 vol.3.

[11] A. Watt, *VLF Radio Engineering*, ser. International series of monographs on electromagnetic waves. Pergamon Press, 1967.

[12] H. Wheeler, "Fundamental limitations of a small vlf antenna for submarines," *IRE Transactions on Antennas and Propagation*, vol. 6, no. 1, pp. 123–125, 1958.

[13] V. Rakov and M. Uman, *Lightning: Physics and Effects*. Cambridge University Press, 2006.

[14] J. Galejs, A. Cullen, V. Fock, and J. Wait, *Terrestrial Propagation of Long Electromagnetic Waves: International Series of Monographs in Electromagnetic Waves*, ser. International series of monographs on electromagnetic waves. Elsevier Science, 2013.

[15] K. Davies and I. of Electrical Engineers, *Ionospheric Radio*, ser. Electromagnetics and Radar Series. Peregrinus, 1990.

[16] D. A. Chrissan and A. C. Fraser-Smith, "A clustering poisson model for characterizing the interarrival times of sferics," *Radio Science*, vol. 38, no. 4, 2003.

[17] R. K. Said, U. S. Inan, and K. L. Cummins, "Long-range lightning geolocation using a vlf radio atmospheric waveform bank," *Journal of Geophysical Research: Atmospheres*, vol. 115, no. D23, 2010.

[18] M. B. Cohen, R. K. Said, E. W. Paschal, J. C. McCormick, N. C. Gross, L. Thompson, M. Higginson-Rollins, U. S. Inan, and J. Chang, "Broadband longwave radio remote sensing instrumentation," *Review of Scientific Instruments*, vol. 89, no. 9, p. 094 501, 2018.

[19] M. B. Cohen, U. S. Inan, and E. W. Paschal, "Sensitive Broadband ELF/VLF Radio Reception With the AWESOME Instrument," *IEEE Transactions on Geoscience and Remote Sensing*, vol. 48, no. 1, pp. 3–17, 2010.

[20] S. K. Harriman, E. W. Paschal, and U. S. Inan, "Magnetic sensor design for femtotesla low-frequency signals," *IEEE Transactions on Geoscience and Remote Sensing*, vol. 48, no. 1, pp. 396–402, 2010.

[21] A. Tronson, "Single-chip vlf magnetic field receiver," PhD thesis, Stanford University, 2014.

[22] H. C. Séran and P. Fergeau, "An optimized low-frequency three-axis search coil magnetometer for space research," *Review of Scientific Instruments*, vol. 76, no. 4, p. 044 502, 2005.

[23] M. Parrot, D. Benoist, J. Berthelier, J. Błecki, Y. Chapuis, F. Colin, F. Elie, P. Fergeau, D. Lagoutte, F. Lefeuvre, C. Legendre, M. Lévêque, J. Pinçon, B. Poirier, H.-C. Seran, and P. Zamora, "The magnetic field experiment imsc and its data processing onboard demeter: Scientific objectives, description and first results," *Planetary and Space Science*, vol. 54, no. 5, pp. 441 –455, 2006, First Results of the DEMETER Micro-Satellite.

[24] M. Füllekrug, "Wideband digital low-frequency radio receiver," *Measurement Science and Technology*, vol. 21, no. 1, p. 015 901, 2009.

[25] A. C. Fraser-Smith and R. A. Helliwell, "The stanford university elf/vlf radiometer project: Measurement of the global distribution of elf/vlf electromagnetic noise," in *1985 IEEE International Symposium on Electromagnetic Compatibility*, 1985, pp. 1–7.

[26] E. W. Paschal, "The design of broad-band VLF receivers with air-core loop antennas," STARLab, Stanford University, Tech. Rep., 1980.

[27] B. V. Gurses, K. T. Whitmore, and M. Cohen, "Electric field sensor design for longwave radio reception," in *2019 SoutheastCON*, 2019, pp. 1–2.

[28] B. V. Gurses, K. T. Whitmore, and M. B. Cohen, "Ultra-sensitive broadband remote sensing instrument for longwave radio reception," *Earth and Space Science Open Archive*, pp. 1–8, 2020.

[29] P. S. Carter, "Circuit Relations in Radiating Systems and Applications to Antenna Problems," *Proceedings of the Institute of Radio Engineers*, vol. 20, no. 6, pp. 1004–1041, 1932.

[30] G. Vasilescu, *Electronic Noise and Interfering Signals: Principles and Applications*. Berlin, Germany: Springer, 2005.

[31] M. Cohen, M. Golkowski, U. Inan, and J. DeSilva, "WALDO! A Massive Public Repository of Global ELF/VLF Radio Data," *Earth and Space Science Open Archive*, p. 1, 2020.

[32] D. M. Hull, S. J. Vinci, and Yongming Zhang, "ARL Electric-field Cage Modeling, Design and Calibration," in *2006 12th Biennial IEEE Conference on Electromagnetic Field Computation*, 2006, pp. 89–89.